JACS Au
AN OPEN ACCESS JOURNAL OF THE AMERICAN CHEMICAL SOCIETY



pubs.acs.org/jacsau
Article

# Weak-Field Electro-Flash Induced Asymmetric Catalytic Sites toward Efficient Solar Hydrogen Peroxide Production

Fangshuai Chen, Ximeng Lv, Haozhen Wang, Fan Wen, Liangti Qu, Gengfeng Zheng,* and Qing Han*

Cite This: *JACS Au* 2024, 4, 1219−1228
Read Online

ACCESS | Metrics & More | Article Recommendations | Supporting Information

**ABSTRACT:** Borocarbonitride (BCN), in a mesoscopic asymmetric state, is regarded as a promising photocatalyst for artificial photosynthesis. However, BCN materials reported in the literature primarily consist of symmetric N-$[B]_3$ units, which generate highly spatial coupled electron−hole pairs upon irradiation, thus kinetically suppressing the solar-to-chemical conversion efficiency. Here, we propose a facile and fast weak-field electro-flash strategy, with which structural symmetry breaking is introduced on key nitrogen sites. As-obtained double-substituted BCN (*ds*-BCN) possesses high-concentration asymmetric $[B]_2$−N-C coordination, which displays a highly separated electron−hole state and broad visible-light harvesting, as well as provides electron-rich N sites for $O_2$ affinity. Thereby, *ds*-BCN delivers an apparent quantum yield of 7.6% at 400 nm and a solar-to-chemical conversion efficiency of 0.3% for selective 2e-reduction of $O_2$ to $H_2O_2$, over 4-fold higher than that of the traditional calcined BCN analogue and superior to the metal-free $C_3N_4$-based photocatalysts reported so far. The weak-field electro-flash method and as-induced catalytic site symmetry-breaking methodologically provide a new method for the fast and low-cost fabrication of efficient nonmetallic catalysts toward solar-to-chemical conversions.

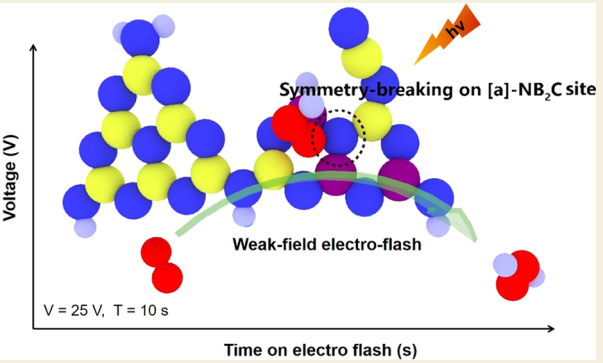


**KEYWORDS:** *weak-field electro-flash strategy, asymmetric catalytic site, borocarbonitride, photocatalysis, hydrogen peroxide*

## INTRODUCTION

Two-dimensional (2D) nonmetallic conjugated polymers, e.g., polymeric carbon nitride ($C_3N_4$) or boron nitride (BN) materials, have recently attracted growing research interest as a new generation of multifunctional materials.[1−3] However, highly symmetrical molecular structures of these 2D polymers usually result in delocalized electron states, which may suppress electron enrichment in photocatalytic reactions. Moreover, the relatively poor ability toward water oxidation also significantly hinders the hole-involving half-reaction and limits the solar-to-chemical conversion (SCC) efficiency in water. To overcome these issues, a structural symmetry-breaking strategy is employed to destroy the delocalization states and enhance carrier generation and enrichments.[4,5] For instance, borocarbonitride (BCN) in an asymmetrical motif state (i.e., the B-rich zone and C-rich zone coexist in a molecule) is a promising photocatalytic candidate with a wide spectrum of changes in the electronic structure and charge-transfer resistance and has been successfully applied in water splitting and $CO_2$ reduction.[6,7] To date, mechanism studies have revealed that the unique N−B structures in BCN catalysts generally exhibit localized electron states, thus enriching the electron density on the N sites.[8,9] As a result, the adsorption along with activation of reactants (e.g., $O_2$, $CO_2$, etc.) would be enhanced, and the subsequent proton-coupled electron transfer could be kinetically accelerated for a higher product (i.e., $H_2O_2$ or other fuels) yield. In addition, the introduction of B atoms significantly optimizes the valence band level of the catalysts, thus promoting the oxidation half-reaction,[8] with which the SCC efficiency will be higher. However, it remains a huge challenge to clearly identify the catalytic performance of different N−B structures in BCN, and oriented coordination-symmetry-breaking on specific catalytic sites (i.e., catalytic site asymmetry) could hardly be achieved.

To obtain adequate BCN catalysts, diverse methods including laser ablation, pyrolysis, chemical vapor deposition, and dc arc discharge have been presented.[10,11] However, the harsh conditions (e.g., high temperature (700−1000 °C), long reaction time (5−9 h), and strict gas atmosphere), along with a slow rate (~5 K $min^{-1}$) in the heating and cooling stage, required by these methods usually lead to sluggish crystallization. Therefore, the formation of symmetrical N-$[B]_3$ units (i.e., *h*-BN-like structure), which is thermodynamically more

Received: January 26, 2024
Revised: February 14, 2024
Accepted: February 16, 2024
Published: March 5, 2024

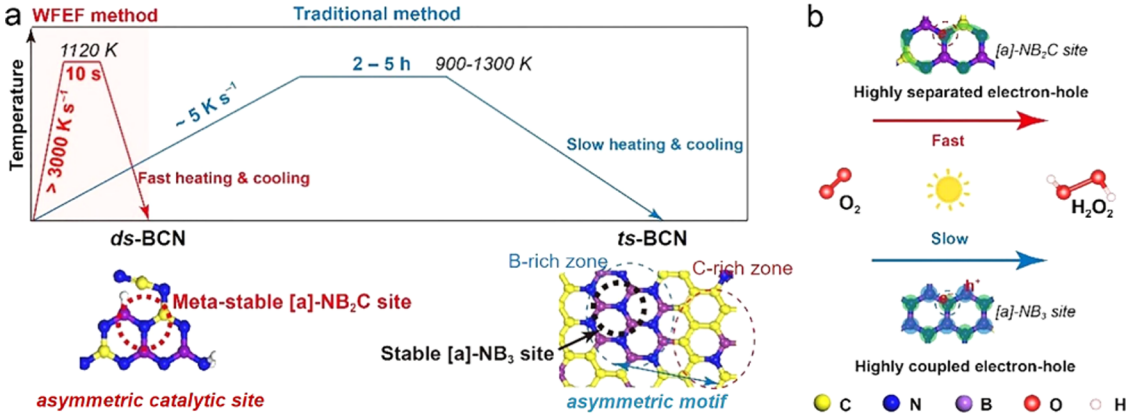


**Figure 1.** Structure–activity relation on different BCN catalysts. (a) Schematic illustration of the WFEF method and traditional calcining method for fabricating *ds*-BCN with an asymmetric catalytic site and *ts*-BCN with an asymmetric motif, respectively. (b) Differences between *ds*-BCN and *ts*-BCN toward photocatalytic $O_2$-to-$H_2O_2$ conversion.

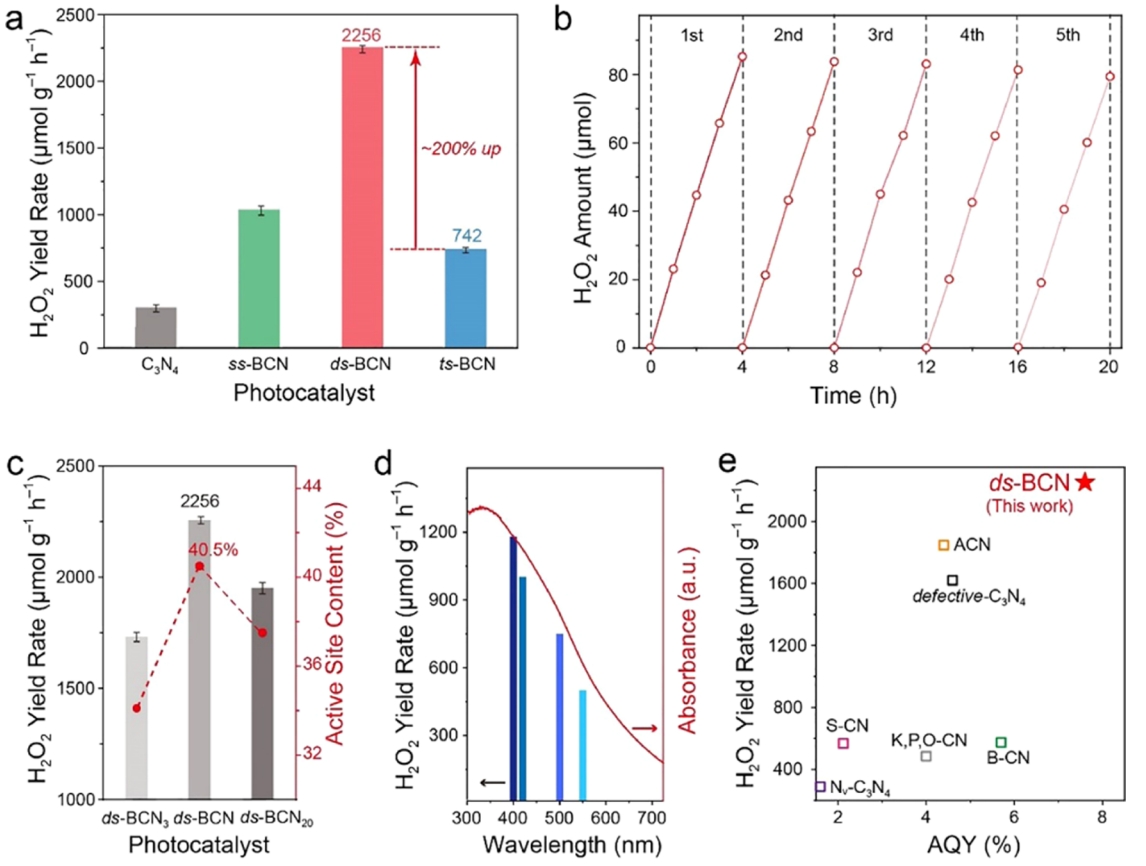


**Figure 2.** Performance in photocatalytic $O_2$-to-$H_2O_2$ conversion. (a) Photocatalytic $H_2O_2$ production activities of $C_3N_4$, *ss*-BCN, *ds*-BCN, and *ts*-BCN ($\lambda > 400$ nm). (b) Photocatalytic $H_2O_2$ yield rate of *ds*-BCN for 20 h ($\lambda > 400$ nm). (c) Photocatalytic $H_2O_2$ production activity on *ds*-BCN with different contents of [a]-$NB_2C$ sites prepared by varying the WFEF treatment times (i.e., 3, 10, and 20 s). (d) Wavelength-dependent $H_2O_2$ production on *ds*-BCN. (e) $H_2O_2$ production rate and AQY for *ds*-BCN in comparison with other doping and defect engineering on $C_3N_4$-based photocatalysts (Note: detailed information is provided in Table S3).

stable,[12] is usually dominant, and BCN catalysts with enriched triple-substituted coedge N sites (i.e., [a]-$NB_3$) are thus obtained (marked as *ts*-BCN, Figure 1a, bottom right). Although the reported BCN materials have the asymmetry motif state, the symmetrical [a]-$NB_3$ coordination on these BCN materials displays a significantly coupled electron–hole structure upon light irradiation (Figure 1b, lower), which generally suppresses the carrier transfer and thereby slackens photoreduction.[13,14] In contrast, a coordination-symmetry-breaking structure could prevent the formation of a highly coupling state and thus enhance the photocatalytic performance.[15] According to previous studies, thermal shock[16] or electric shock[17] would result in an explosive crystallization with an enriched metastable phase, which provides an opportunity for asymmetric structure generation.[4,18]

Herein, we present a facile weak-field electro-flash (WFEF) method for manufacturing BCN materials with symmetry-breaking catalytic sites in the air. In this process, extremely fast


https://doi.org/10.1021/jacsau.4c00076
JACS Au 2024, 4, 1219–1228

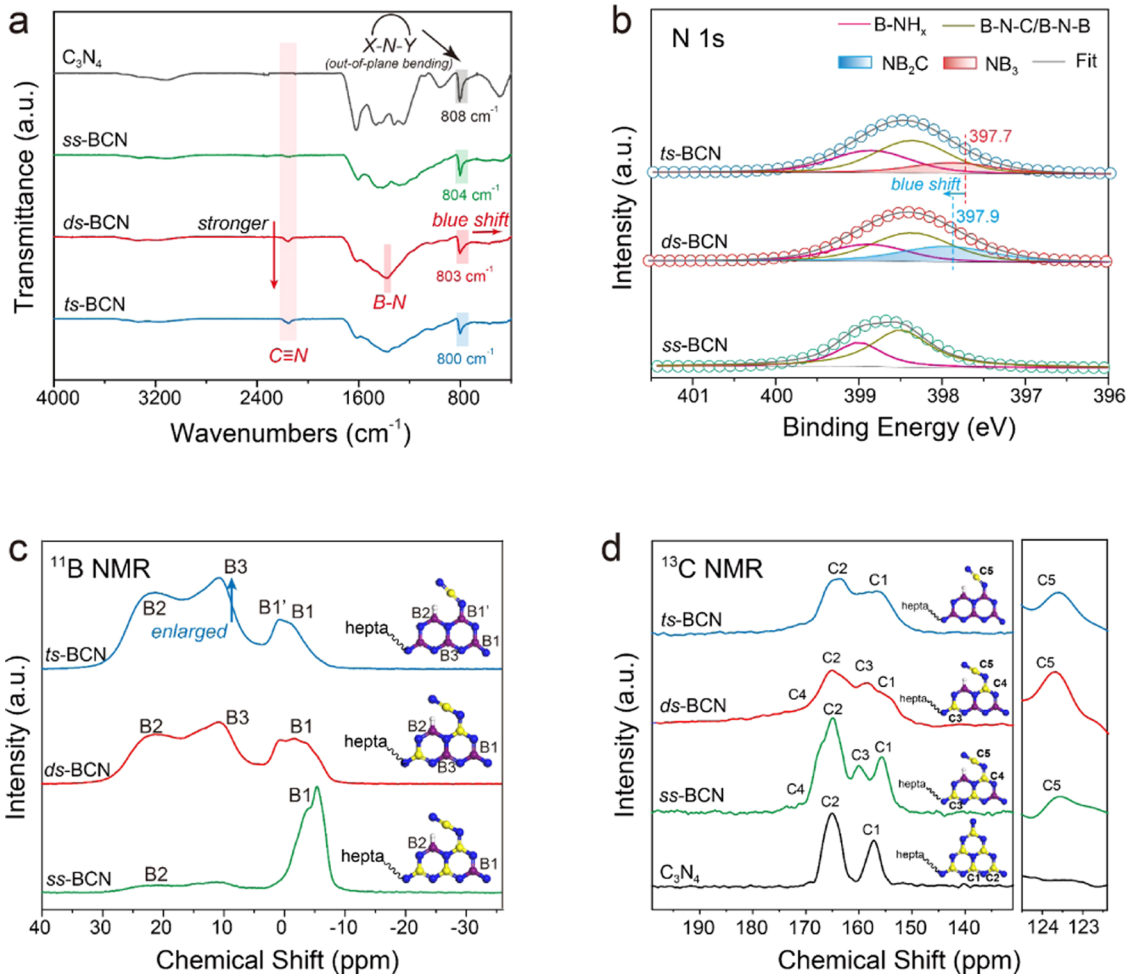


**Figure 3.** Structural characterizations. (a) FTIR spectra of $C_3N_4$, *ss*-BCN, *ds*-BCN, and *ts*-BCN. (b) High-resolution N 1s spectra of *ss*-BCN, *ds*-BCN, and *ts*-BCN. (c) Solid-state $^{11}$B MAS NMR spectra of *ss*-BCN, *ds*-BCN, and *ts*-BCN (inset: molecular structure; hepta refers to the heptazine ring). (d) Solid-state $^{13}$C MAS NMR spectra of $C_3N_4$, *ss*-BCN, *ds*-BCN, and *ts*-BCN.

heating (>3000 K s$^{-1}$) at 25 V leads to explosive crystallization, and a metastable double-substituted BCN (*ds*-BCN, Figure 1a, bottom left) is synthesized. In the metastable *ds*-BCN structure, highly active asymmetric [B]$_2$−N-C (i.e., [a]-NB$_2$C) coordinations with localized electron states are formed (Figure 1b, upper), which feature lower exciton binding energy, extend the visible-light response, and accelerate $O_2$ adsorption. To elucidate the catalytic site structure, single-substituted [B]−N-C$_2$ (i.e., [a]-NBC$_2$) coordinations with less localized electron states are prepared by the WFEF method and designed as *ss*-BCN. We tested the performance of photocatalytic $H_2O_2$ production for WFEF materials (*ds*-BCN and *ss*-BCN) against the traditional calcined BCN with symmetric N-[B]$_3$ units (*ts*-BCN). Both *ds*-BCN and *ss*-BCN exhibited excellent photocatalytic performance, in particular, *ds*-BCN displayed a more sustained $H_2O_2$ production than its *ts*-BCN analogue and was more active than $C_3N_4$ and its derivates reported.

## RESULTS AND DISCUSSION

### Photocatalytic Activity on *ds*-BCN

The WFEF method is utilized to construct asymmetric N−B structures (Figure 1a). For example, a fine powder with a weight ratio for dicyandiamide/sodium borohydride of 7.5:1 was suspended on top of a carbon cloth holder connected with the electrodes of a stable DC power supply. The solid-state explosive crystallization reaction was performed with a voltage of 25 V for 10 s. The reaction temperature can instantaneously reach 1120 K with a heating rate of ∼3000 K s$^{-1}$ (Figure S1) with the simultaneous release of $H_2$ during the explosive reaction, leading to the in situ generation of flake-like *ds*-BCN with a yield of ∼85 wt % (Figures S2e,f and S3). The Brunauer−Emmett−Teller (BET) surface area of *ds*-BCN was measured to be 51 m$^2$ g$^{-1}$, and the pore size was less than 10 nm (Figure S4). Interestingly, the strong-field electro-flash (SFEF) method generates BCN materials enriched with a symmetrical [a]-NB$_3$ structure,[19] similar to the traditional calcined BCN (*ts*-BCN) (Figure S2g,h). By changing the dicyandiamide content (i.e., the weight ratio of dicyandiamide/sodium borohydride is 30:1), a sample with different N sites of [a]-NBC$_2$ is obtained, which was designated as *ss*-BCN (Figure S2c,d). Meanwhile, $C_3N_4$ was also prepared by thermal polymerization for comparison (Figure S2a,b).

The photocatalytic $H_2O_2$ production performance was first investigated in the presence of benzyl alcohol as a sacrificial agent under $\lambda$ > 400 nm irradiation. As shown in Figure 2a, the $H_2O_2$ production rate of *ds*-BCN (2256 $\mu$mol h$^{-1}$ g$^{-1}$) is 200% higher than that of *ts*-BCN (742 $\mu$mol h$^{-1}$ g$^{-1}$) and also higher than those of *ss*-BCN (1038 $\mu$mol h$^{-1}$ g$^{-1}$) and $C_3N_4$ (420


https://doi.org/10.1021/jacsau.4c00076
JACS Au 2024, 4, 1219−1228

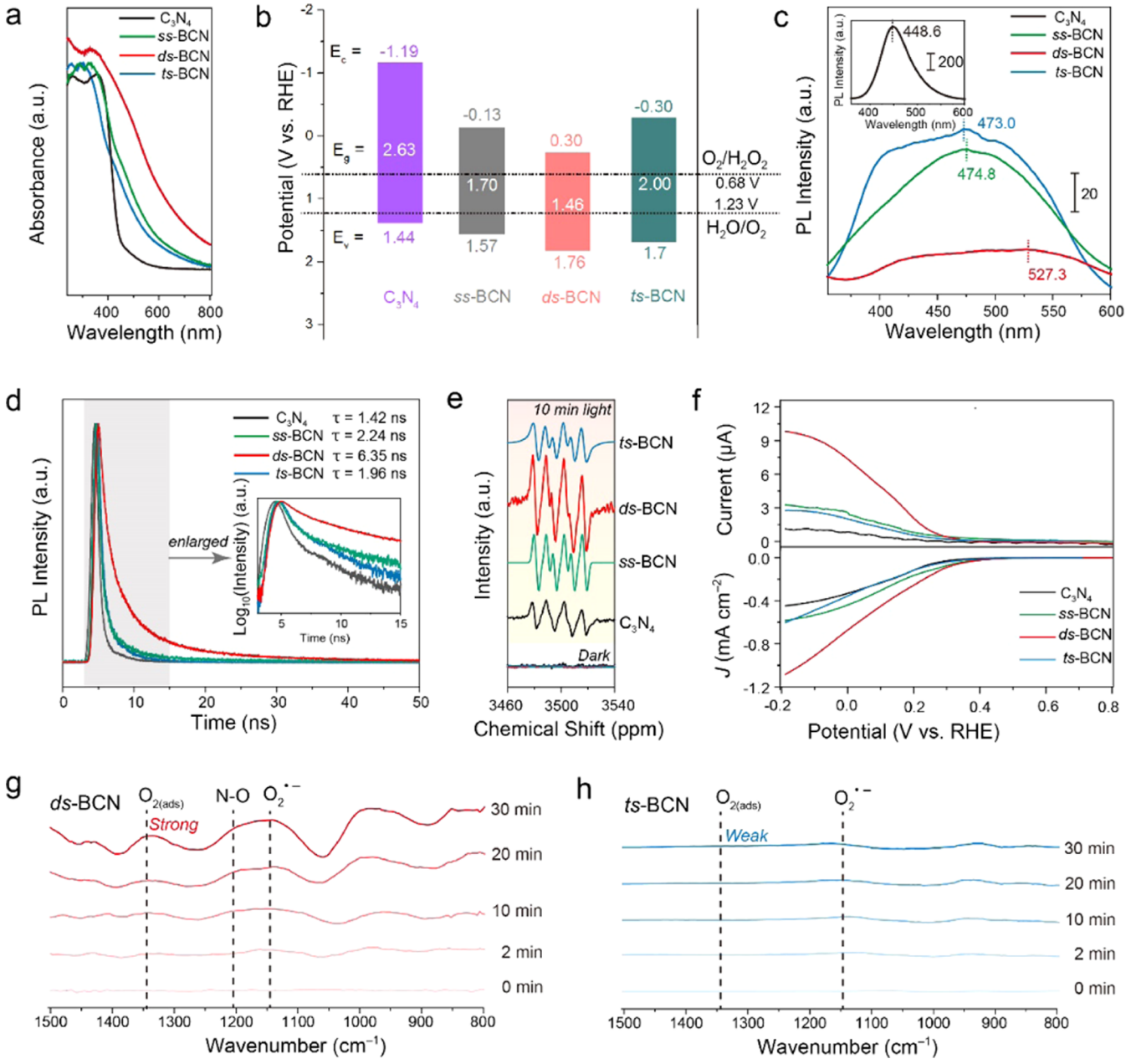


**Figure 4.** Mechanistic study based on spectral experiments. (a) UV−vis absorption spectra of $C_3N_4$, *ss*-BCN, *ds*-BCN, and *ts*-BCN. (b) Band structure alignments for $C_3N_4$, ss-BCN, ds-BCN, and ts-BCN. (c) PL spectra of $C_3N_4$, *ss*-BCN, *ds*-BCN, and *ts*-BCN, with the excitation wavelength of 360 nm. (d) TRPL spectra of $C_3N_4$, *ss*-BCN, *ds*-BCN, and *ts*-BCN. (e) EPR spectra of $C_3N_4$, *ss*-BCN, *ds*-BCN, and *ts*-BCN tested in ultrapure water under an $O_2$ atmosphere. (f) RRDE polarization curves recorded at 1600 rpm in 0.1 M phosphate-buffered saline for $C_3N_4$, *ss*-BCN, *ds*-BCN, and *ts*-BCN. In situ DRIFT spectra of (g) *ds*-BCN and (h) *ts*-BCN.

$\mu$mol $h^{-1}$ $g^{-1}$). This result suggests that the symmetry-breaking catalytic sites have a significant effect on the photocatalytic performance, which was further studied by comparing the photocatalytic activities of *ds*-BCN samples with different contents of the asymmetric [a]-$NB_2C$ sites. A series of *ds*-BCN samples were synthesized by varying the WFEF treatment times (from 3s, 10s, to 20s), with the resulting samples denoted as *ds*-$BCN_3$, *ds*-BCN, and *ds*-$BCN_{20}$ (Figure S5a), respectively. It was found that all of the *ds*-BCN samples show a higher photocatalytic $H_2O_2$ production rate compared with *ts*-BCN (Figure 2a,c). *ds*-BCN also exhibits stable $H_2O_2$ production without performance degradation (Figure 2b) or structural and compositional changes (Figure S6 and Tables S1, S2) for five cycles lasting 20 h, indicating its robust photochemical stability. Moreover, the $H_2O_2$ production activity of the *ds*-BCN samples is correlated well with the increase in the relative content of the asymmetric [a]-$NB_2C$ sites (Figure 2c). Close analysis showed that the relative content of the [a]-$NB_2C$ sites in the best sample of *ds*-BCN is up to 40.5% (Figure S5b), which could significantly optimize the electronic structures and redox energies. These results suggest that the WFEF method is an efficient technique for the fast and controllable fabrication of the asymmetric [a]-$NB_2C$ structure in conjugated polymers. $H_2O_2$ can scarcely be detected over *ds*-BCN (Figure S7) when there is no irradiation, no $O_2$, or no photocatalyst, implying that the formation of


https://doi.org/10.1021/jacsau.4c00076
JACS Au 2024, 4, 1219−1228

$H_2O_2$ is a photocatalytic $O_2$ reduction process. Wavelength-dependent $H_2O_2$ production of *ds*-BCN matches its optical absorption spectrum, further suggesting that it is a light-driven reaction (Figure 2d). The calculated apparent quantum efficiency (AQY) of *ds*-BCN is 7.6% at 400 nm, substantially higher than the previous results obtained from doping and defect engineering on $C_3N_4$-based photocatalysts (Figure 2e, Table S3). Furthermore, the photocatalytic $H_2O_2$ production without sacrificial agents was also investigated for *ds*-BCN (Figure S8a), which shows a considerable $H_2O_2$ evolution rate of 292 $\mu$mol $h^{-1}$ $g^{-1}$ with an SCC efficiency of 0.30%, over four times higher than that of its *ts*-BCN analogue (0.07%, Figure S8b) and surpassing those of the metal-free $C_3N_4$-based photocatalysts reported so far (Table S4).[20]

## Characterization of *ds*-BCN

The structure of *ds*-BCN was first studied by powder X-ray diffraction (XRD). Different from two distinctive peaks at about 13.1° (in-plane structural packing motif) and 27.5° (interlayer stacking) in $C_3N_4$ (Figure S9),[21,22] the peak corresponding to in-plane structural packing motif disappears in *ss*-BCN, *ds*-BCN, and *ts*-BCN, suggesting the destruction of heptazine units.[23,24] Compared with $C_3N_4$, the Fourier transform infrared (FTIR) spectrum of *ds*-BCN presents a blue-shift at ~803 $cm^{-1}$ (i.e., the out-of-plane bending mode of X−N-Y in heptazine rings, X,Y= C or B), and a new B−N vibration peak at 1374 $cm^{-1}$ can be observed, suggesting the introduction of B atoms in hepatazine units (Figure 3a).[25] Moreover, *ss*-BCN, *ds*-BCN, and *ts*-BCN have a new peak at 2161 $cm^{-1}$, typical of the stretching vibration of cyanogroups,[26−28] suggesting an obvious ring-opening reaction in the heptazine rings.

X-ray photoelectron spectroscopy (XPS) was performed to analyze the chemical states of the photocatalysts (Figure S10). The N 1s XPS spectrum of *ds*-BCN shows three peaks at 400.3, 398.9, and 398.2 eV, corresponding to N−C, N═C, and N−B, respectively,[29,30] whereas no N−B can be detected in $C_3N_4$ (Figure S10b). The N−B peak of *ds*-BCN was higher than that of *ss*-BCN, indicating that there are more B−N structures in *ds*-BCN (26.5%) than in *ss*-BCN (12.7%). However, the N−B peak in *ts*-BCN showed a decrease (24.2%), which may be caused by a kinetically slower formation of [a]-$NB_3$. This decrease can also be confirmed by elemental analysis (Table S1). Further subdivision of the N−B group to illustrate the differences in the BCN catalysts (Figure 3b) shows that *ss*-BCN exhibits B-$NH_x$ (398.9 eV) and B−N−C (398.4 eV) and *ds*-BCN and *ts*-BCN show a similar peak at 398.9 eV (B-$NH_x$).[31] The slight shift of B−N−C in *ds*-BCN to lower binding energies results from the formation of B−N−B when more B was introduced, and a new peak at 397.9 eV belonging to the $NB_xC_y$ is observed in *ds*-BCN. In contrast to *ss*-BCN, the *ts*-BCN showed a new peak at 397.7 eV, which is ascribed to $NB_xC_y$. The observed blue-shift of the $NB_xC_y$ peak (~0.2 eV, Figure 3b) in the N 1s spectra of ds-BCN revealed the formation of electron-rich $NB_2C$ coordinates (i.e., the N−$B_2C$ coordinate weighs more than N−$B_3$ in *ds*-BCN), which could prevent the formation of highly coupling electron−hole pairs and thus enhance the photocatalytic performance.

Solid-state $^{11}B$ magic-angle spinning nuclear magnetic resonance (MAS NMR) spectroscopy was performed to further investigate the structure of *ds*-BCN. As shown in Figure 3c, *ss*-BCN, *ds*-BCN, and *ts*-BCN all display three peaks at −4.7, 12.4, and 22.3 ppm, which are ascribed to $N_2$−B−$NH_2$ (B1), N═B(H)−N (B2), and B−$N_3$ (B3),[32,33] respectively. It should be noted that a new B1′ peak ($N_2$−B-N(C)) arises at ~0 ppm because of the ring-opening reaction with the introduction of B dopants in *ts*-BCN, suggesting an increase in a new type of bay-site B atoms. Furthermore, the intensity of the B1′ peak is stronger than that of the B1 peak in *ts*-BCN, which results in the increased intensity of the B3 peak being markedly different from that of *ds*-BCN, indicating the formation of an *h*-BN-like structure.

The $^{13}C$ MAS NMR spectrum of $C_3N_4$ (Figure 3d) shows two peaks at 157.2 and 165.0 ppm ascribed to N═C−$N_2$ (C1) and N═C−N($NH_x$) (C2) in the heptazine units.[30] New peaks at 160.0 (C3) and 123.6 (C5) ppm and the widened peak of $N_2$−C−N(C≡N) (C4) are observed for *ss*-BCN and *ds*-BCN, which can be attributed to the B substitution reaction-induced ring-opening to form $N_2$−C═N(B), $N_2$−C═N(C≡N), and cyanogroups,[8] respectively. Furthermore, *ds*-BCN shows the strongest peak intensity of the cyanogroup and nearly disappearing peak of C1, which suggests that more B atoms substitute C atoms in the heptazine heterocycles, in accordance with the variation trend of B content (Figure S10d). Moreover, *ts*-BCN presents only two peaks at 157.2 ppm (C1) and 165.0 ppm (C2), which indicates the preserved $C_3N_4$-like C species in *ts*-BCN, further confirming the coexistence of the enriched symmetric [a]-$NB_3$ sites (i.e., *h*-BN-like structure) and the original $C_3N_4$ frameworks.

## Spectra-Based Mechanism on [a]-$NB_2C$ Sites

To gain insights into the molecular mechanism, a series of spectrum experiments were then conducted. The ultraviolet−visible (UV−vis) absorption spectrum (Figure 4a) of the light-yellow $C_3N_4$ (Figure S11) presents an absorption edge at about 471 nm, corresponding to the band gap of 2.63 eV. In contrast, the rich-yellow *ss*-BCN and the light-brown *ts*-BCN exhibit a slight red shift in the 410−800 nm region, while the bark-brown *ds*-BCN shows a strong bathochromic shift in the 380−800 nm region, suggesting the superficial B doping for *ss*-BCN and homogeneous B substitution for *ds*-BCN. The individual band gaps of *ss*-BCN, *ds*-BCN, and *ts*-BCN were found to be 1.70, 1.46, and 2.00 eV, respectively, by extrapolating the linear region of the Tauc plots (Figure S12a). As determined from the valence band (VB) XPS spectra (Figure S12b), the VB maxima of $C_3N_4$, *ss*-BCN, *ds*-BCN, and *ts*-BCN are 2.00, 2.13, 2.32, and 2.26 eV (vs RHE), respectively. Together with the calculated bandgap values, the band positions of the obtained samples are summarized in Figure 4b. It can be seen that the reduction levels for $O_2/H_2O_2$ and $H_2O/O_2$ are well positioned in the middle of the band gap, which indicates that the reduction and oxidation processes are energetically possible.[34] The more positive VBM shift of *ds*-BCN caused by B substitution indicates a high driving force for water photooxidation, in accordance with its higher currents and lower onset potentials of the 4-electron water oxidation pathway (Figures S13 and S14). Furthermore, the narrowed band gap of 1.46 eV for *ds*-BCN favors visible-light harvesting, which can also be confirmed by a photoluminescence (PL) spectrum where the emission peak of *ds*-BCN is red-shifted relative to $C_3N_4$ (Figure 4c).

The PL signal intensity gradually decreases from $C_3N_4$, *ts*-BCN, and *ss*-BCN, to *ds*-BCN (Figure 4c), and the decline of PL signals is correlated well with the increase in the relative content of the asymmetric [a]-$NB_2C$ sites (Figure S15),


https://doi.org/10.1021/jacsau.4c00076
JACS Au 2024, 4, 1219−1228

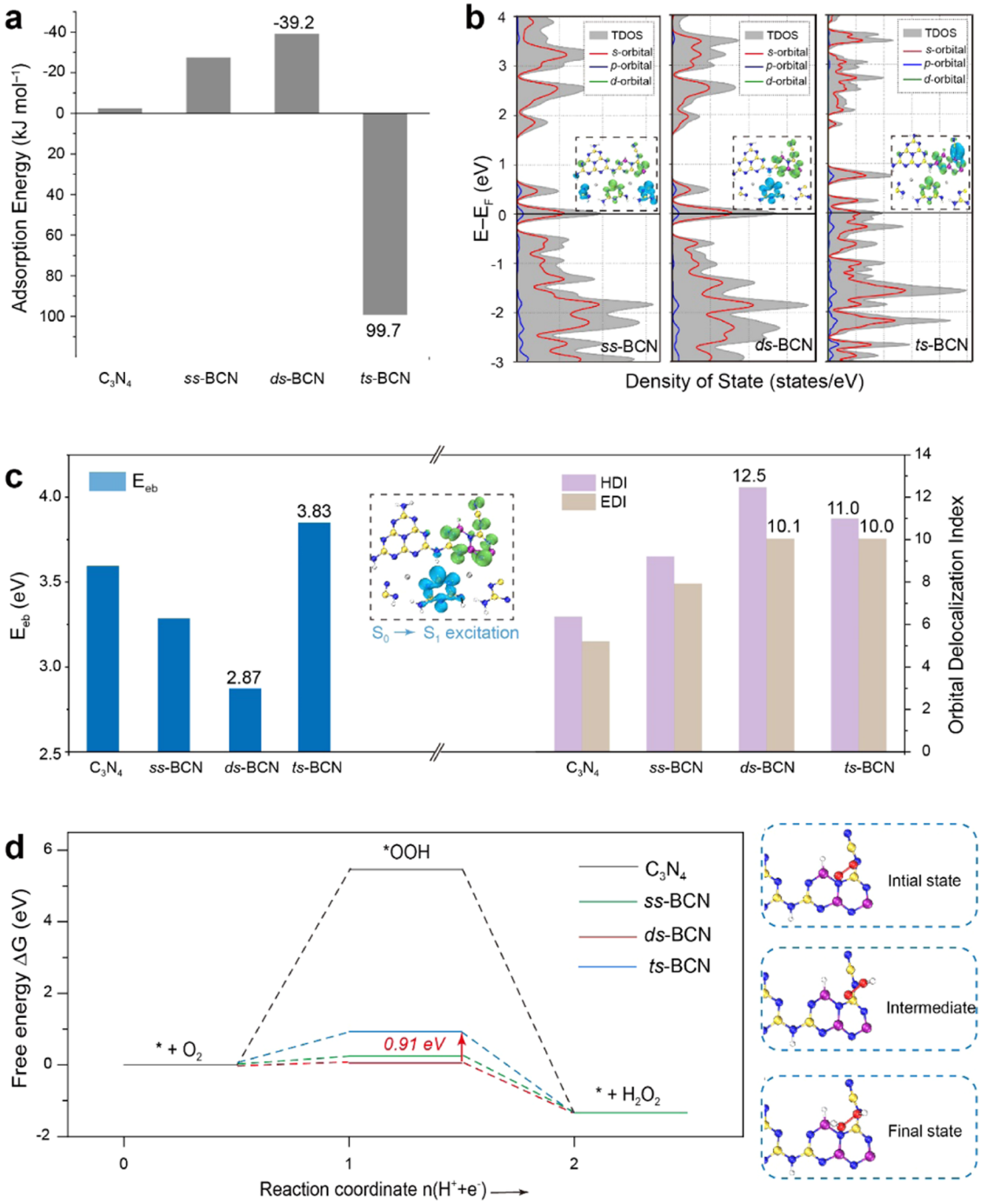


**Figure 5.** Theoretical calculations. (a) Adsorption energy of $O_2$ on $C_3N_4$, *ss*-BCN, *ds*-BCN, and *ts*-BCN. (b) DOS of *ss*-BCN, *ds*-BCN, and *ts*-BCN. Electron−hole distribution of *ss*-BCN, *ds*-BCN, and *ts*-BCN in the first excited states are shown in the inset (green isosurface: electron distribution; blue isosurface: hole distribution). (c) Exciton binding energy, electron delocalization index (EDI), and hole delocalization index (HDI) values of $C_3N_4$, *ss*-BCN, *ds*-BCN, and *ts*-BCN. (d) Free-energy diagram for $O_2$-to-$H_2O_2$ conversions on different catalysts. The schematic illustration of the initial, intermediate, and final states shows the adsorption model of each step.

indicating that the radiative recombination of electron−hole pairs has been effectively suppressed due to the B substitution and the formation of the metastable [a]-$NB_2C$ site-induced electronic localization, which leads to efficient charge separation. Meanwhile, *ds*-BCN shows the highest photocurrent intensity and smallest semicircle in the Nyquist plot (Figure S16) in comparison to $C_3N_4$, *ss*-BCN and *ts*-BCN, further suggesting effectively enhanced charge separation and transport.[35] Time-resolved PL (TRPL) decay spectroscopy was further performed to determine the charge separation properties. As shown in Figure 4d and Table S5, the electron average lifetime of *ds*-BCN is 6.35 ns, significantly longer than those of *ss*-BCN (2.24 ns), *ts*-BCN (1.96 ns) and $C_3N_4$ (1.42 ns), which indicates that high-concentration asymmetric [a]-$NB_2C$ sites efficiently enhance the charge separation efficiency. Electrostatic potential surface maps (Figure S17) clearly reveal that B introduction in heptazine units of *ds*-BCN results in a remarkable symmetry breaking on the catalytic N sites, thus


https://doi.org/10.1021/jacsau.4c00076
JACS Au 2024, 4, 1219−1228

inducing a stronger intramolecular electrostatic potential (i.e., pyridine nitrogen at the broken site owns a negative potential) and facilitating charge separation and transfer.

To confirm the reactive oxygen species during the photosynthesis of $H_2O_2$, electron paramagnetic resonance (EPR) technology was performed using 5,5-dimethyl-1-pyrroline N-oxide (DMPO) as the spin-trap agent. As shown in Figure 4e, the six strong characteristic signals for DMPO-$^{\bullet}O_2^-$ are observed on *ds*-BCN under light irradiation, which are absent in the dark, but much higher than those of $C_3N_4$, *ss*-BCN, and *ts*-BCN, implying that the asymmetric [a]-$NB_2C$ sites effectively promote the formation of $^{\bullet}$OOH intermediates. The rotating disk electrode test result indicates that the average electron transfer number of ORR for *ds*-BCN is 2.1 (Figure S18), which indicates a two-step single-electron route.[36] Furthermore, *ds*-BCN exhibits higher current and lower onset potential compared with $C_3N_4$, *ss*-BCN, and *ts*-BCN (Figure 4f), which illustrates that faster ORR kinetics occur on the asymmetric [a]-$NB_2C$ sites of *ds*-BCN. As a result, *ds*-BCN displays an obviously higher $H_2O_2$ selectivity of ~83% than those of $C_3N_4$ (~66%), *ss*-BCN (~74%), and *ts*-BCN (~71%) (Figure S19). In situ diffuse reflectance infrared Fourier transform (DRIFT) spectroscopy shows that *ds*-BCN (Figure 4g) displays obvious vibrational peaks at about 1343, 1206, and 1145 $cm^{-1}$ corresponding to O−O, N−O and $^{\bullet}O_2^-$ species along with an increase in irradiation time.[37] Moreover, the peaks of the O−O and $^{\bullet}O_2^-$ of *ds*-BCN are higher than that of *ts*-BCN (Figure 4h), and the N−O peak is not detected in *ts*-BCN, which strongly suggests that [a]-$NB_2C$ sites on *ds*-BCN lead to significant enhancement in $O_2$ activation.

### Theoretical Calculations

Density functional theory (DFT) calculations were also performed to reveal the internal mechanism of superior catalytic performance in *ds*-BCN. By employing several typical sites in $C_3N_4$, *ss*-BCN, *ds*-BCN, and *ts*-BCN to assess $O_2$ adsorption ability (Figure S20), it can be found that *ds*-BCN has the tightest-bounded state at [a]-$NB_2C$ site with an adsorption energy ($E_{ad}$) of −39.17 kJ·$mol^{-1}$, indicating that the initiation site of ORR might be [a]-$NB_2C$ (Figure 5a and Table S5). This adsorption energy is larger than those on $C_3N_4$ (−2.49 kJ·$mol^{-1}$), *ss*-BCN (−27.49 kJ·$mol^{-1}$), and especially *ts*-BCN (>80 kJ·$mol^{-1}$), indicating the formation of a necessary stably adsorbed state in the *ds*-BCN framework for ORR (Table S5). Furthermore, the temperature-programmed desorption of $O_2$ ($O_2$-TPD) shows that ds-BCN has a stronger $O_2$ adsorption capacity than $C_3N_4$, ss-BCN, and ts-BCN (Figure S21), which indicates that the introduction of the [a]-$NB_2C$ site into *ds*-BCN can drastically increase the $O_2$ adsorption capacity, in agreement with the calculation conclusions. A higher effective mass of electrons ($m^*$) at the conduction band minimum can be observed with the introduction of B atoms, i.e., $m^*$ = 9.32, 11.71, and 10.50 for *ss*-BCN, *ds*-BCN, and *ts*-BCN, respectively (Table S5). Meanwhile, the density of state (DOS) around the Fermi level is significantly increased after the introduction of B dopants. These two findings both suggest a localized electron state in *ds*-BCN materials, which might be a key factor accounting for the enhanced $O_2$ adsorption and as-promoted ORR performance.[38,39] Furthermore, the enlarged DOS around the Fermi level for *ds*-BCN with a narrow band gap also indicates the potential for faster electron−hole separation. The excitation state analyses proved the highly separated electron−hole configuration in *ss*-BCN and *ds*-BCN (inset in Figure 5b). Enriched photogenerated electrons are majorly located at N sites in the heptazine ring-like [a]-$NB_2C$, suggesting the potential for photocatalytic reduction on these N sites. In contrast, a highly coupled electron−hole structure can be observed in *ts*-BCN (inset in Figure 5b) and $C_3N_4$ (Figure S22), suggesting a poor electron−hole separation efficiency for these two catalysts.

The Bader charge analyses were also performed for models with negative $E_{ad}$, indicating that the amount of charge transferred from the catalyst to $O_2$ exhibits an increase of 2 orders of magnitude on *ds*-BCN compared with $C_3N_4$ (i.e., $-10.31 \times 10^{-3}$|e| vs $-0.41 \times 10^{-3}$|e|; Table S5). Further assessment of the $S_0 \rightarrow S_1$ excitation in these catalysts also provides some information on the unique electron state in *ds*-BCN. The exciton binding energy ($E_{eb}$) in *ds*-BCN (2.87 eV) is significantly smaller than that in other systems (3.60 eV for CN, 3.29 eV for *ss*-BCN, and 3.83 eV for *ts*-BCN, Figure 5c), implying a more stabilized electron−hole pair on *ds*-BCN.[14] The electron delocalization index (EDI) and the hole delocalization index (HDI) are also notably larger in *ds*-BCN (i.e., EDI ~ 10.1, HDI ~ 12.5; Figure 5c and Table S6), further suggesting that localized electrons in *ds*-BCN may be the key reason accounting for this stabilization effect. With such a stabilization effect, the photosynthetic efficiency is promoted,[40,41] i.e., the *ds*-BCN structure exhibits the lowest Gibbs free energy toward crucial $^{\bullet}$OOH intermediate ($\Delta G$ = 0.09 eV), resulting in an accelerated ORR-to-$H_2O_2$ conversion compared with *ts*-BCN ($\Delta G$ = 1.00 eV), $C_3N_4$ ($\Delta G$ = 5.46 eV), or *ss*-BCN ($\Delta G$ = 0.25 eV) (Figure 5d). Taken together, the introduction of [a]-$NB_2C$ coordination in *ds*-BCN led to a remarkable symmetry breaking and significantly changed the original delocalization state in the heptazine units to a localized one. Therefore, well-separated electron−hole pairs can be stabilized in such a localized system, and $O_2$-to-reactive oxygen species (ROS) conversion and subsequent $H_2O_2$ production on electron-rich N atoms can be easily achieved through the acquirement of more electrons.

## CONCLUSIONS

In summary, we present a weak-field electro-flash approach for the facile and quick synthesis of BCN materials made of heptazine domains along with high-concentration catalytic site asymmetry of [a]-$NB_2C$ coordination. The proposed *ds*-BCN was obtained in only 10 s by simply mixing and electro-flashing the reagents in air, which is particularly suitable for fast, low-cost, and mass fabrication. As-obtained *ds*-BCN with the optimized [a]-$NB_2C$ site content exhibits over 5-fold higher $H_2O_2$ production than $C_3N_4$ and much higher than those of the reported metal-free $C_3N_4$-based photocatalysts. Our research of the system revealed that the superior activity of the catalyst may originate from the coordination-symmetry-breaking structure with a broadened visible-light spectrum, on which stable electron−hole pairs, enhanced $O_2$ adsorption, and $2e^-$ reduction can be achieved. This work not only provides a powerful weak-field electro-flash approach strategy for oriented asymmetric catalytic site fabrication, meaningful for the oriented syntheses of functional conjugated polymers, but also sheds light on the structure−activity relationship of the nonmetallic BCN photocatalytic process.



https://doi.org/10.1021/jacsau.4c00076
JACS Au 2024, 4, 1219−1228

## EXPERIMENTAL SECTION

### Syntheses of *ds*-BCN and *ss*-BCN

A mixture of $C_2H_4N_4$ and $NaBH_4$ with a mass ratio of 7.5:1 was ground finely and placed on the CC holder connected with a cheap DC power supply (MAISHENG, 0−30 A, 0−30 V, Price: a few tens of dollars). The *ds*-BCN samples were synthesized after applying an output voltage of 25 V for 3, 10, and 20 s in air, respectively. For comparison, *ss*-BCN was prepared by changing the mass ratio (30:1) of the mixed powder of $C_2H_4N_4$ and $NaBH_4$. The obtained samples were washed with ethanol and deionized water to remove the impurity.

### Synthesis of *ts*-BCN

The traditional *ts*-BCN was synthesized by heating the mixture of $C_2H_4N_4$ and $NaBH_4$ in a weight ratio of 7.5:1 from room temperature to 850 °C in $N_2$ with a ramp rate of 5 °C/min, stabilized for 4 h, and then cooled to room temperature. The obtained sample was washed with ethanol and deionized water to remove the impurity.

### Photocatalytic Production of $H_2O_2$

Ten milligrams of the as-prepared catalyst were dispersed in 48 mL of deionized water containing 2 mL of benzyl alcohol. The suspension was bubbled with $O_2$ in the dark for 30 min before irradiation. A 300 W Xe lamp (Micosolar 300, Beijing Perfectlight Technology Co. Ltd., China) with $\lambda > 400$ nm was used as the light source. The temperature of the reaction system was maintained at 20 ± 0.5 °C during the experiment. After the photocatalytic reaction, 1 mL of the reaction liquid was filtered and then mixed with the as-prepared $Ce(SO_4)_2$ solution. Then, the concentration of the produced $H_2O_2$ was analyzed by a precolored UV−vis spectrophotometry method (details in the Supporting Information).

## ASSOCIATED CONTENT

### Supporting Information

The Supporting Information is available free of charge at https://pubs.acs.org/doi/10.1021/jacsau.4c00076.

Experimental details, characterization, electrochemical data, and DFT calculations (PDF)

## AUTHOR INFORMATION


### Corresponding Authors

**Gengfeng Zheng** − *Laboratory of Advanced Materials, Department of Chemistry and Shanghai Key Laboratory of Molecular Catalysis and Innovative Materials, Faculty of Chemistry and Materials Science, Fudan University, Shanghai 200438, P. R. China;* orcid.org/0000-0002-1803-6955; Email: gfzheng@fudan.edu.cn

**Qing Han** − *Laboratory of Advanced Materials, Department of Chemistry and Shanghai Key Laboratory of Molecular Catalysis and Innovative Materials, Faculty of Chemistry and Materials Science, Fudan University, Shanghai 200438, P. R. China;* orcid.org/0009-0004-5235-975X; Email: qhan@fudan.edu.cn

### Authors

**Fangshuai Chen** − *Laboratory of Photoelectronic/Electrophotonic Conversion Materials, Key Laboratory of Cluster Science, Ministry of Education of China, School of Chemistry and Chemical Engineering, Beijing Institute of Technology, Beijing 100081, P. R. China*

**Ximeng Lv** − *Laboratory of Advanced Materials, Department of Chemistry and Shanghai Key Laboratory of Molecular Catalysis and Innovative Materials, Faculty of Chemistry and Materials Science, Fudan University, Shanghai 200438, P. R. China;* orcid.org/0000-0002-0482-2349

**Haozhen Wang** − *Laboratory of Advanced Materials, Department of Chemistry and Shanghai Key Laboratory of Molecular Catalysis and Innovative Materials, Faculty of Chemistry and Materials Science, Fudan University, Shanghai 200438, P. R. China*

**Fan Wen** − *Laboratory of Photoelectronic/Electrophotonic Conversion Materials, Key Laboratory of Cluster Science, Ministry of Education of China, School of Chemistry and Chemical Engineering, Beijing Institute of Technology, Beijing 100081, P. R. China*

**Liangti Qu** − *Key Laboratory of Organic Optoelectronics & Molecular Engineering of Ministry of Education, Department of Chemistry, Tsinghua University, Beijing 100084, P. R. China;* orcid.org/0000-0002-0161-3816

Complete contact information is available at: https://pubs.acs.org/10.1021/jacsau.4c00076


### Author Contributions

F.C. and X.L. contributed equally to this work. F.C.: data curation, investigation, writing the original draft; X.L.: data analysis, DFT calculation, and writing—review and editing; H.W. and F.W.: data curation and formal analysis; L.Q.: formal analysis and writing—review and editing; G.Z.: formal analysis, funding acquisition, resources, and writing—review and editing; Q.H.: conceptualization, formal analysis, funding acquisition, resources, supervision, and writing—review and editing. All authors have given approval to the final version of the manuscript. CRediT: **Fangshuai Chen** data curation, investigation, writing-original draft; **Ximeng Lv** formal analysis, writing-review & editing; **Haozhen Wang** data curation, formal analysis; **Fan Wen** data curation, formal analysis; **Liangti Qu** formal analysis, writing-review & editing; **Gengfeng Zheng** formal analysis, funding acquisition, resources, writing-review & editing; **Qing Han** conceptualization, formal analysis, funding acquisition, resources, supervision, writing-review & editing.

### Notes

The authors declare no competing financial interest.

## ACKNOWLEDGMENTS

This work was supported by the National Natural Science Foundation of China (22222901, 22175022, 22025502, and U23A20552), the Science and Technology Commission of Shanghai Municipality (21DZ1206800, 19XD1420400), the Shanghai Municipal Education Commission (2019-01-07-00-07E00045), the National Key Research and Development Program of China (2018YFA0209401), and the China Postdoctoral Science Found (2023M730637 and 2023TQ0082). The computations in this research were performed using the CFFF platform of Fudan University.

## REFERENCES

(1) Teng, Z.; Zhang, Q.; Yang, H.; Kato, K.; Yang, W.; Lu, Y. R.; Liu, S.; Wang, C.; Yamakata, A.; Su, C.; Liu, B.; Ohno, T. Atomically dispersed antimony on carbon nitride for the artificial photosynthesis of hydrogen peroxide. *Nat. Catal.* **2021**, *4*, 374−384.

(2) Yang, R.; Fan, Y.; Mei, L.; Shin, H. S.; Voiry, D.; Lu, Q.; Li, J.; Zeng, Z. Synthesis of atomically thin sheets by the intercalation-based exfoliation of layered materials. *Nat. Synth.* **2023**, *2*, 101−118.

(3) Zhao, Y.; Zhang, P.; Yang, Z.; Li, L.; Gao, J.; Chen, S.; Xie, T.; Diao, C.; Xi, S.; Xiao, B.; Hu, C.; Choi, W. Mechanistic analysis of multiple processes controlling solar-driven $H_2O_2$ synthesis using engineered polymeric carbon nitride. *Nat. Commun.* **2021**, *12*, No. 3701.
(4) Di, J.; Jiang, W.; Liu, Z. Symmetry breaking for semiconductor photocatalysis. *Trends Chem.* **2022**, *4*, 1045−1055.
(5) Zhan, H.; Zhou, Q.; Li, M.; Zhou, R.; Mao, Y.; Wang, P. Photocatalytic $O_2$ activation and reactive oxygen species evolution by surface B-N bond for organic pollutants degradation. *Appl. Catal., B* **2022**, *310*, No. 121329.
(6) Luo, Z.; Fang, Y.; Zhou, M.; Wang, X. A borocarbonitride ceramic aerogel for photoredox catalysis. *Angew. Chem., Int. Ed.* **2019**, *58*, 6033−6037.
(7) Rao, C. N. R.; Chhetri, M. Borocarbonitrides as metal-free catalysts for the hydrogen evolution reaction. *Adv. Mater.* **2019**, *31*, No. e1803668.
(8) Zhao, D.; Dong, C. L.; Wang, B.; Chen, C.; Huang, Y. C.; Diao, Z.; Li, S.; Guo, L.; Shen, S. Synergy of dopants and defects in graphitic carbon nitride with exceptionally modulated band structures for efficient photocatalytic oxygen evolution. *Adv. Mater.* **2019**, *31*, No. e1903545.
(9) Tian, Z.; Zhang, Q.; Thomsen, L.; Gao, N.; Pan, J.; Daiyan, R.; Yun, J.; Brandt, J.; López-Salas, N.; Lai, F.; Li, Q.; Liu, T.; Amal, R.; Lu, X.; Antonietti, M. Constructing interfacial boron-nitrogen moieties in turbostratic carbon for electrochemical hydrogen peroxide production. *Angew. Chem., Int. Ed.* **2022**, *61*, No. e202206915.
(10) Bahadur, R.; Singh, G.; Bando, Y.; Vinu, A. Advanced porous borocarbonitride nanoarchitectonics: Their structural designs and applications. *Carbon* **2022**, *190*, 142−169.
(11) Rao, C. N. R.; Gopalakrishnan, K. Borocarbonitrides, $B_xC_yN_z$: Synthesis, characterization, and properties with potential applications. *ACS Appl. Mater. Interfaces* **2017**, *9*, 19478−19494.
(12) Chhetri, M.; Maitra, S.; Chakraborty, H.; Waghmare, U. V.; Rao, C. N. R. Superior performance of borocarbonitrides, $B_xC_yN_z$, as stable, low-cost metal-free electrocatalysts for the hydrogen evolution reaction. *Energy Environ. Sci.* **2016**, *9*, 95−101.
(13) Li, Y.; Wang, W.; Wang, Y.; He, H.; Yu, X.; Xia, D.; Deng, L.; Liu, Y. Edge engineering of carbon nitride for enhanced sacrificial agent-free photocatalytic $H_2O_2$ evolution. *Chem. Eng. Sci.* **2023**, *282*, No. 119333.
(14) Di, X.; Lv, X.; Wang, H.; Chen, F.; Wang, S.; Zheng, G.; Wang, B.; Han, Q. Enhanced pre-sensitization in metal-free covalent organic frameworks promoting hydrogen peroxide photosynthesis. *Chem. Eng. J.* **2023**, *455*, No. 140124.
(15) Huang, C.; Chen, C.; Zhang, M.; Lin, L.; Ye, X.; Lin, S.; Antonietti, M.; Wang, X. Carbon-doped BN nanosheets for metal-free photoredox catalysis. *Nat. Commun.* **2015**, *6*, No. 7698.
(16) Liu, C.; Zhou, W.; Zhang, J.; Chen, Z.; Liu, S.; Zhang, Y.; Yang, J.; Xu, L.; Hu, W.; Chen, Y.; Deng, Y. Air-assisted transient synthesis of metastable nickel oxide boosting alkaline fuel oxidation reaction. *Adv. Energy Mater.* **2020**, *10*, No. 2001397.
(17) Jiang, T.; Liu, Z.; Yuan, Y.; Zheng; Park, X. S.; Wei, S.; Li, L.; Ma, Y.; Liu, S.; Chen, J.; Zhu, Z.; Meng, Y.; Li, K.; Sun, J.; Peng, Q.; Chen, W. Ultrafast electrical pulse synthesis of highly active electrocatalysts for beyond-industrial-level hydrogen gas batteries. *Adv. Mater.* **2023**, *35*, No. 2300502.
(18) Zhang, X.; Yan, P.; Xu, J.; Li, F.; Herold, F.; Etzold, B. J. M.; Wang, P.; Su, D.; Lin, S.; Qi, W.; Xie, Z. Methanol conversion on borocarbonitride catalysts: Identification and quantification of active sites. *Sci. Adv.* **2022**, *6*, No. eaba5778.
(19) Chen, W.; Li, J.; Ge, C.; Yuan, Z.; Algozeeb, W. A.; Advincula, P. A.; Gao, G.; Chen, J.; Ling, K.; Choi, C. H.; McHugh, E. A.; Wyss, K. M.; Luong, D. X.; Wang, Z.; Han, Y.; Tour, J. M. Turbostratic boron−carbon−nitrogen and boron nitride by flash joule heating. *Adv. Mater.* **2022**, *34*, No. 2202666.
(20) Tan, H.; Zhou, P.; Liu, M.; Zhang, Q.; Liu, F.; Guo, H.; Zhou, Y.; Chen, Y.; Zeng, L.; Gu, L.; Zheng, Z.; Tong, M.; Guo, S. Photocatalysis of water into hydrogen peroxide over an atomic Ga-$N_5$ site. *Nat. Synth.* **2023**, *2*, 557−563.
(21) Cai, J.; Huang, J.; Wang, S.; Iocozzia, J.; Sun, Z.; Sun, J.; Yang, Y.; Lai, Y.; Lin, Z. Crafting mussel-inspired metal nanoparticle-decorated ultrathin graphitic carbon nitride for the degradation of chemical pollutants and production of chemical resources. *Adv. Mater.* **2019**, *31*, No. 1806314.
(22) Kang, Y.; Yang, Y.; Yin, L.; Kang, X.; Liu, G.; Cheng, H. An amorphous carbon nitride photocatalyst with greatly extended visible-light-responsive range for photocatalytic hydrogen generation. *Adv. Mater.* **2015**, *27*, 4572−4577.
(23) Majdoub, M.; Anfar, Z.; Amedlous, A. Emerging Chemical Functionalization of g-$C_3N_4$: Covalent/Noncovalent Modifications and Applications. *ACS Nano* **2020**, *14*, 12390−12469.
(24) Han, Q.; Wang, B.; Zhao, Y.; Hu, C.; Qu, L. A graphitic-$C_3N_4$ "seaweed" architecture for enhanced hydrogen evolution. *Angew. Chem., Int. Ed.* **2015**, *54*, 11433−11437.
(25) Lin, W.; Chen, H.; Lin, G.; Yao, S.; Zhang, Z.; Qi, J.; Jing, M.; Song, W.; Li, J.; Liu, X.; Fu, J.; Dai, S. Creating frustrated Lewis pairs in defective boron carbon nitride for electrocatalytic nitrogen reduction to ammonia. *Angew. Chem., Int. Ed.* **2022**, *61*, No. e202207807.
(26) Wang, W.; Zhang, H.; Zhang, S.; Liu, Y.; Wang, G.; Sun, C.; Zhao, H. Potassium-ion-assisted regeneration of active cyano groups in carbon nitride nanoribbons: Visible-light-driven photocatalytic nitrogen reduction. *Angew. Chem., Int. Ed.* **2019**, *58*, 16644−16650.
(27) Han, Q.; Wang, B.; Gao, J.; Cheng, Z.; Zhao, Y.; Zhang, Z.; Qu, L. Atomically thin mesoporous nanomesh of graphitic $C_3N_4$ for high-efficiency photocatalytic hydrogen evolution. *ACS Nano* **2016**, *10*, 2745−2751.
(28) Zhang, X.; Ma, P.; Wang, C.; Gan, L.; Chen, X.; Zhang, P.; Wang, Y.; Li, H.; Wang, L.; Zhou, X.; Zheng, K. Unravelingthe dual defect sites in graphite carbon nitride for ultra-high photocatalytic $H_2O_2$ evolution. *Energy Environ. Sci.* **2022**, *15*, 830−842.
(29) Lei, W.; Portehault, D.; Dimova, R.; Antonietti, M. Boron carbon nitride nanostructures from salt melts: tunable water-soluble phosphors. *J. Am. Chem. Soc.* **2011**, *133*, 7121−7127.
(30) Wang, W.; Zhou, H.; Liu, Y.; Zhang, S.; Zhang, Y.; Wang, G.; Zhang, H.; Zhao, H. Formation of B-N-C coordination to stabilize the exposed active nitrogen atoms in g-$C_3N_4$ for dramatically enhanced photocatalytic ammonia synthesis performance. *Small* **2020**, *16*, No. 1906880.
(31) Giusto, P.; Arazoe, H.; Cruz, D.; Lova, P.; Heil, T.; Aida, T.; Antonietti, M. Boron carbon nitride thin films: From disordered to ordered conjugated ternary materials. *J. Am. Chem. Soc.* **2020**, *142*, 20883−20891.
(32) Bai, X.; Zhang, X.; Sun, Y.; Huang, M.; Fan, J.; Xu, S.; Li, H. Low ruthenium content confined on boron carbon nitride as an efficient and stable electrocatalyst for acidic oxygen evolution reaction. *Angew. Chem., Int. Ed.* **2023**, *62*, No. e202308704.
(33) Shamsabadi, T.; Fattahimoghaddam, H.; Lee, B.; Ryu, H.; Jang, J. Caesium sites coordinated in boron-doped porous and wrinkled graphitic carbon nitride nanosheets for efficient charge carrier separation and Transfer: Photocatalytic $H_2$ and $H_2O_2$ production. *Chem. Eng. J.* **2021**, *423*, No. 130067.
(34) Krishnaraj, C.; Jena, H. S.; Bourda, L.; Laemont, A.; Pachfule, P.; Roeser, J.; Chandran, C. V.; Borgmans, S.; Rogge, S. M. J.; Leus, K.; Stevens, C. V.; Martens, J. A.; Speybroeck, V. V.; Breynaert, E.; Thomas, A.; Voort, P. V. D. Strongly reducing (diarylamino)benzene-based covalent organic framework for metal-free visible light photocatalytic $H_2O_2$ generation. *J. Am. Chem. Soc.* **2020**, *142*, 20107−20116.
(35) Zhao, D.; Wang, Y.; Dong, C.; Huang, Y.; Chen, J.; Xue, F.; Shen, S.; Guo, L. Meso-structured Platinum Thin Films: Boron-doped nitrogen-deficient carbon nitride-based Z-scheme heterostructures for photocatalytic overall water splitting. *Nat. Energy* **2021**, *6*, 388−397.
(36) Wu, C.; Teng, Z.; Yang, C.; Chen, F.; Yang, H.; Wang, L.; Xu, H.; Liu, B.; Zheng, G.; Han, Q. Polarization engineering of covalent triazine frameworks for highly efficient photosynthesis of hydrogen


https://doi.org/10.1021/jacsau.4c00076
JACS Au 2024, 4, 1219−1228

peroxide from molecular oxygen and water. *Adv. Mater.* **2022**, *34*, No. 2110266.
(37) Zhi, Q.; Liu, W.; Jiang, R.; Zhan, X.; Jin, Y.; Chen, X.; Yang, X.; Wang, K.; Cao, W.; Qi, D.; Jiang, J. Piperazine-linked metal-phthalocyanine frameworks for highly efficient visible-light-driven $H_2O_2$ photosynthesis. *J. Am. Chem. Soc.* **2022**, *144*, 21328−21336.
(38) Kong, S.; Lv, X.; Wang, X.; Liu, Z.; Li, Z.; Jia, B.; Sun, D.; Yang, C.; Liu, L.; Guan, A.; Wang, J.; Zheng, G.; Huang, F. Delocalization state-induced selective bond breaking for efficient methanol electrosynthesis from $CO_2$. *Nat. Catal.* **2023**, *6*, 6−15.
(39) Fang, Y.; Lv, X.; Lv, Z.; Wang, Y.; Zheng, G.; Huang, F. Electron-extraction engineering induced 1T''-1T' phase transition of $Re_{0.75}V_{0.25}Se_2$ for ultrafast sodium ion storage. *Adv. Sci.* **2022**, *9*, No. 2205680.
(40) Yang, T.; Zhang, H.; Zhan, C.; Liang, L.; Xu, Y.; Ruan, P.; Zhang, Y.; Li, J.; Wang, L.; Lv, X.; Yang, S.; Pao, C.; Huang, X. Strong synergy between single atoms and single-atom alloys enables active and selective $H_2O_2$ synthesis. *Chem. Catal.* **2022**, *2*, 3607−3620.
(41) Li, Q.; Jiao, Y.; Tang, Y.; Zhou, J.; Wu, B.; Jiang, B.; Fu, H. Shear stress triggers ultrathin-nanosheet carbon nitride assembly for photocatalytic $H_2O_2$ produciton coupled with selective alcohol oxidation. *J. Am. Chem. Soc.* **2023**, *145*, 20837−20848.



https://doi.org/10.1021/jacsau.4c00076
*JACS Au* 2024, 4, 1219−1228